

Long-term continuous monitoring of the diffuse attenuation coefficient at 490 nm from global oceans using combined SeaWiFS and MODISA data

Jingfan Li, Jun Chen & Wenting Quan

To cite this article: Jingfan Li, Jun Chen & Wenting Quan (2024) Long-term continuous monitoring of the diffuse attenuation coefficient at 490 nm from global oceans using combined SeaWiFS and MODISA data, International Journal of Remote Sensing, 45:5, 1539-1555, DOI: [10.1080/01431161.2024.2314004](https://doi.org/10.1080/01431161.2024.2314004)

To link to this article: <https://doi.org/10.1080/01431161.2024.2314004>



Published online: 15 Feb 2024.



Submit your article to this journal [↗](#)



View related articles [↗](#)



View Crossmark data [↗](#)



Long-term continuous monitoring of the diffuse attenuation coefficient at 490 nm from global oceans using combined SeaWiFS and MODISA data

Jingfan Li^a, Jun Chen^a and Wenting Quan^b

^aKey Laboratory of Physical Electronics and Devices, Ministry of Education, Faculty of Electronic and Information Engineering, Xi'an Jiaotong University, Xi'an, China; ^bShaanxi Meteorological Service Center of Agricultural Remote Sensing and Economic Crop, Xi'an, China

ABSTRACT

To enhance the long-term monitoring ability of multi-sourced remote sensing data, we needed to minimize the inter-mission biases between the data retrieved from different satellites. We evaluated three existing diffuse attenuation coefficients at 490 nm ($K_d(490)$) using nine independent datasets collected from the global oceans. The results indicate that the updated neural network-based four-band $K_d(490)$ retrieval model (updated-NFKM) decreased the uncertainty by > 4% from the NASA official $K_d(490)$ retrieval model (NOKM) and the inherent optical properties-based $K_d(490)$ retrieval model (IOPK). Specifically, matchup analysis showed that the updated-NFKM model produced < 40% uncertainty in deriving $K_d(490)$ from MODISA and SeaWiFS data, and the uncertainty of SeaWiFS-predicted $K_d(490)$ was ~ 5% lower than the MODISA-predicted $K_d(490)$. Using the updated-NFKM model, >80% of the global ocean had an uncertainty for $K_d(490)$ estimates that were lower than 30%, while the model performed much better for the Western Pacific, Arctic Ocean, and Northern Atlantic compared to the Eastern Pacific, South Ocean, and Southern Atlantic. To enable a naturally smooth transition from SeaWiFS to MODISA-observed $K_d(490)$ products, it was critical to cross-calibrate the inter-mission difference. The results show that using the cross-calibration models proposed in this study, the MODISA-predicted $K_d(490)$ accounted for > 86% of the variations of SeaWiFS-predicted $K_d(490)$, even though the empirical coefficients of the cross-calibration model had to be adjusted according to the time scales of the composite remote sensing data. Finally, we used the cross-calibration model to minimize the time series of SeaWiFS and MODISA-predicted $K_d(490)$ data. Our results indicate that the $K_d(490)$ values gradually increased in the low-latitude regions during past two decades.

ARTICLE HISTORY

Received 21 October 2023
Accepted 17 January 2024

KEYWORDS

Heat stratification; upper oceanic layer; turbid water; solar heating; integrated attenuation coefficient model

1. Introduction

Managing marine resources requires systematically evaluating water properties. Water clarity is a common indicator of water quality and can be denoted by the diffuse

CONTACT Jun Chen ✉ chenjun@xjtu.edu.cn Key Laboratory of Physical Electronics and Devices, Ministry of Education, Faculty of Electronic and Information Engineering, Xi'an Jiaotong University, No. 28, Xianning Road, Xi'an 710049, China

attenuation coefficient for downwelling irradiance (Zhao et al. 2013). This index retrieves the photosynthetically active radiation at various depths critical to marine organisms such as phytoplankton, coral, and sea grass communities (Masini et al. 1995; Pedersen, Gallegos, and Nielsen 2012; Saulquin et al. 2013). Although capable of providing accurate measurements, using traditional ship-based monitoring of water properties is costly and time consuming, and thus the limited data gathered at sea is highly temporally and spatially variable (Gordon 2019). Conversely, advances in ocean colour satellite technology have opened new opportunities for understanding biogeochemical and physical processes in marine ecosystems at high spatial and temporal scales (Clavano, Boss, and Lee 2007). Satellite observations of the diffuse attenuation coefficient at 490 nm, $K_d(490)$ effectively provides large-scale views of $K_d(490)$ at high spatial and temporal resolutions (Xing et al. 2020), and large-scale surface features such as $K_d(490)$ can now be synoptically mapped for global oceanic and coastal waters (Huang and Yao 2017).

Since the launch of the Coastal Zone Color Scanner (CZCS) in 1978, the ocean colour community has been able to provide global maps of $K_d(490)$ at improved spatial and temporal resolutions compared to field measurements (Barale 1987). More recently, the launch of the Sea-viewing Wide Field-of-view Sensor (SeaWiFS) on 18 September 1997 allowed the global ocean colour dataset to be available in near-real time (Mueller and Trees 1997). SeaWiFS was on a sun-synchronous satellite with a 2801 km swath width, providing 2-day coverage of the global ocean with a nadir resolution of ~ 1 km per pixel (Mueller and Fargion 2002). Shortly after SeaWiFS was launched, the Moderate Resolution Imaging Spectroradiometer broad on Aqua satellite (MODISA) was launched by NASA in 2002. MODISA provides 1-day coverage of global oceanic and coastal waters with a nadir resolution of ~ 1 km per pixel. Using both datasets, oceanographers can understand daily to decadal changes in optical water properties such as $K_d(490)$ over basin or global scales. However, for a particular region, especially coastal zones, the accuracy of long-term trends is often unknown due to the fact that different ocean colour data derived from the different satellites have different uncertainties (Chen et al. 2020; Mélin et al. 2016).

Over the past several decades, there have been many attempts at merging the global or regional time series of the optical parameters from the two different satellite sensors (Chen et al. 2020; Mélin 2016; Sathyendranath et al. 2019). Despite being a well-calibrated and stable sensor (Aiken et al. 1995; Dall'olmo et al. 2005), the SeaWiFS mission was terminated on December 2010 because the mission exceeded its life design. By comparison, there is a general perception that MODISA data are lower quality because of several reported artefacts in sensor design (Meister et al. 2012). However, the MODISA mission is expected to continue into the future to provide the bridge to the defunct SeaWiFS mission. Having MODISA linked to SeaWiFS enhances the long-term monitoring of optical parameters from global oceanic and coastal waters.

To enable a naturally smooth transition from the SeaWiFS to MODISA mission, the biases between these two sensors need to be assessed. The objectives of our study are as follows: (1) to evaluate and compare the accuracy of the NASA official $K_d(490)$ retrieval model (NOKM) proposed by Mueller (2000), the inherent optical properties-based $K_d(490)$ retrieval model (IOPK) proposed by Lee et al. (2013), and the updated neural network-based four-band $K_d(490)$ retrieval model (updated-NFKM) proposed by Chen et al. (2015) in deriving $K_d(490)$ from global oceanic and coastal waters; (2) to evaluate the differences between the MODISA- and SeaWiFS- derived $K_d(490)$; (3) to cross-calibrate the $K_d(490)$

products from MODISA with the SeaWiFS $K_d(490)$ products; (4) to evaluate the uncertainties of the MODISA and SeaWiFS sensors' combined $K_d(490)$ products using field-measured and satellite-observed results; and (5) to understand the monthly trends of $K_d(490)$ from 1997 to 2014 for the global oceans.

2. Data and methods

2.1. Data used

To evaluate the accuracy of the SeaWiFS and MODISA predicted $K_d(490)$, we collected nine independent datasets (Figure 1). The NASA SeaWiFS Project created a large global evaluation dataset consisting of field-measured remote sensing reflectance ($R_{rs}(\lambda)$) at SeaWiFS and MODISA wavelengths and $K_d(490)$ measured using the approach proposed by Mueller et al. (2003). The NASA dataset is known as the SeaBASS dataset (SeaBASS) (NOMAD dataset, $n = 2189$) (Werdel, Bailey, and Werdell 2005). We also used 140 data points from the Yellow and East China Seas from 2003, 104 data points from the East China Sea from 2008 to 2012, 139 data points from the Bohai Sea from 2005, 21 data points from Ariake Bay from 2008 to 2010, 17 data points from Chesapeake Bay from 2009, and 1000 data points from IOCCG reports (IOCCG dataset) (IOCCG 2006). These datasets represent the typical optical properties from global oceanic and coastal waters. To evaluate the accuracy of the satellite-predicted $K_d(490)$ products, we obtained synchronous pairs (340 samples from the MODISA sensor and 514 samples from the SeaWiFS sensor) consisting of satellite-observed $R_{rs}(\lambda)$ and field-measured $K_d(490)$ from SeaBASS and Chinese eastern coastal zones, respectively. To initialize and assess the cross-calibration model for the SeaWiFS- and MODISA- predicted $K_d(490)$ products, we obtained 695 synchronized pairs of SeaWiFS- and MODISA- observed remote sensing reflectance from SeaBASS.

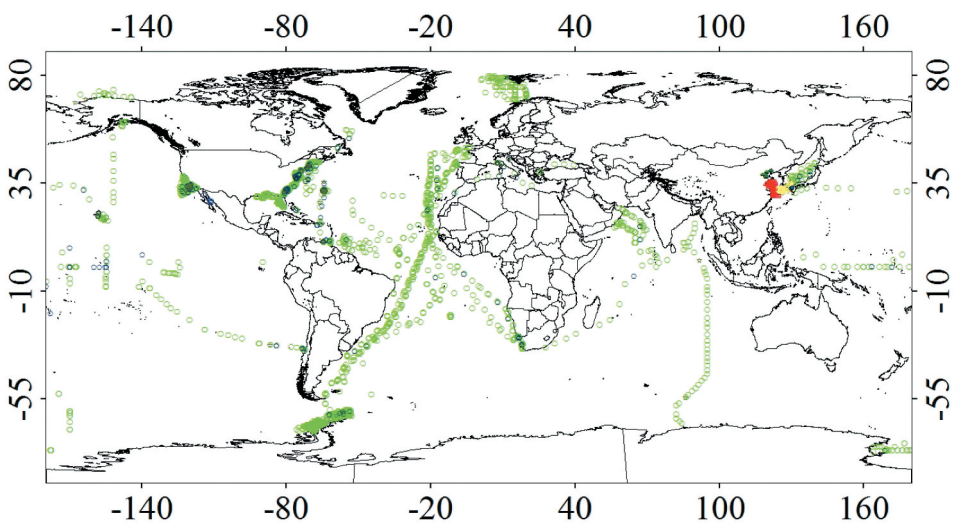


Figure 1. Spatial distribution of field measurements.

2.2. Updating the NFKM Model

Lee et al. (2013) suggested that the Raman factor, RF , could be defined as:

$$RF(\lambda) = \alpha(\lambda) \left[\frac{R^T(443)}{R^T(555)} \right] + \beta(\lambda) [R^T(555)]^{\gamma(\lambda)} \quad (1)$$

where R^T denotes the remote sensing reflectance containing the Raman-scattering contributions; α , β , and γ refer to the corrective factors for the Raman-scattering effects, which are found in Lee et al. (2013). For any given $R^T(\lambda)$ from satellite observations or field measurements, remote sensing reflectance, $R_{rs}(\lambda)$, corrected for the Raman effect, is determined as (Z. Lee et al. 2013):

$$R_{rs}(\lambda) = \frac{R^T(\lambda)}{1 + RF(\lambda)} \quad (2)$$

Due to the fact that satellites and many other sensors measure the remote sensing reflectance above the water surface, we need to convert the above-surface remote sensing reflectance spectral $R_{rs}(\lambda)$ into the below-surface spectral $r_{rs}(\lambda)$ (Z. P. Lee, Carder, and Arnone 2002; Mobley 1994):

$$r_{rs}(\lambda) = \frac{R_{rs}(\lambda)}{0.52 + 1.7R_{rs}(\lambda)} \quad (3)$$

Remote sensing of the diffuse attenuation coefficient is based on the relationship between $r_{rs}(\lambda)$ and the inherent optical properties, namely the ratio of the total back-scattering coefficient to the absorption coefficient $s(\lambda)$ (Gordon 2019):

$$s(\lambda) = \frac{s(\lambda)}{1 + s(\lambda)} \left[I_0 + I_1 \frac{s(\lambda)}{1 + s(\lambda)} \right] \quad (4)$$

where I_0 and I_1 are empirical coefficients, which are found in Lee et al. (2013). Furthermore, we adapt the outputs of the NFKM model used in Chen et al. (2015) to logarithmic values of $s(\lambda)$ (denoted as $\eta(\lambda)$) so that the concept the updated-NFKM model becomes (Chen et al. 2015):

$$K_d(490) = G_N[\eta(443), \eta(488), \eta(555), \eta(667)] \quad (5)$$

where G_N is a neural network function composed of one hidden layer, as shown in Figure 2.

2.3. Statistical evaluation

In this study, we used the root-mean-square of the ratio of the modelled-to-measured values to assess the accuracy of the atmospheric correction. This statistic is referred to as the *MRE* and is described by the following equation:

$$RE_i = \frac{X_{obs,i} - X_{model}}{X_{obs,i}} \times 100\% \quad (6)$$

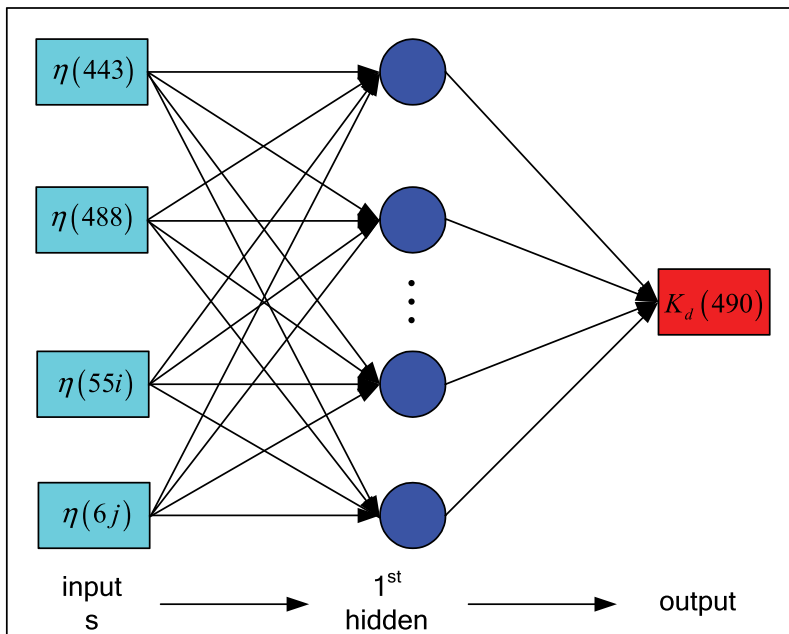


Figure 2. Basic architecture of the updated-NFKM model proposed by Chen et al. (2015), where i and j were 0 and 67, respectively, for the MODISA sensor, and were 5 and 70, respectively, for the SeaWiFS sensor.

$$MRE = \sqrt{\frac{1}{n} \sum_{i=1}^n RE_i^2} \times 100\% \quad (7)$$

where RE_i is the relative uncertainty of the i^{th} observation. $x_{\text{mod},i}$ is the modelled value of the i^{th} element. $x_{\text{obs},i}$ is the observed value of the i^{th} element, and n is the number of elements.

3. Results

3.1. Evaluating the NOKM, IOPK, and updated-NFKM models

The NOKM, IOPK, and updated-NFKM models have been described in detail in the following references (Chen et al. 2015; Z. Lee et al. 2013; Mueller and Trees 1997): The NOKM and IOPK models use global algorithms that have been initialized using global datasets, including the NOMAD and IOCCG datasets (Z. Lee et al. 2013; Mueller and Trees 1997). Much of the literature (Mueller et al. 2003; Saulquin et al. 2013; Zhang et al. 2006) proved that the NOKM and IOPK models are robust for most global oceanic waters and some turbid coastal waters so we did not adjust the coefficients of these models according to the bio-optical datasets. Because there were some adjustments to the inputs of the updated-NFKM model, we retrained the structure and weights with the NOMAD and IOCCG datasets. We used the procedure reported in Chen et al. (2015) to train the weights of the updated-NFKM model. We based the models' evaluation on a comparison of the $K_d(490)$ predicted by these models with the $K_d(490)$ measured analytically for six independent datasets (Figure 1).

Figure 3 shows how well the NOKM, IOPK, and updated-NFKM models derived $K_d(490)$ from our datasets. We found that the MRE of the NOKM $K_d(490)$ prediction was 24.67% for $K_d(490) < 0.3 \text{ m}^{-1}$ ($n = 2660$). When we extrapolated the NOKM model prediction for $K_d(490) > 0.3 \text{ m}^{-1}$ ($n = 950$), the MRE increased to 51.87%. When we applied the NOKM model to all the data, the NOKM model predicted $K_d(490)$ with 33.94% MRE. Fortunately, $K_d(490)$ derived with the IOPK model produced better statistical results than the NOKM model. Particularly, the slope of the linear relationship between the field-measured and model-derived $K_d(490)$ was 0.99, and the corresponding coefficient of determination (R^2) and MRE were 0.81 and 25.57%, respectively. Judging by determination coefficient, the IOPK model could account for 81% of the variation of the $K_d(490)$. However, the IOPK model performed poorly at the low and high values of $K_d(490)$. For example, when we applied the IOPK model to a subsample of 33 pairs for measured $K_d(490) < 0.021 \text{ m}^{-1}$, the model predicted $K_d(490)$ with 55.04% MRE, and when we applied the model to the range $K_d(490) > 1.0 \text{ m}^{-1}$, the model became unstable and many points in the field-measured vs. model-derived $K_d(490)$ scatterplot dispersed were far from the 'one-to-one' line.

By comparison, the updated-NFKM model performed better than the NOKM and IOPK models. When we applied the updated-NFKM model to all the data, the model predicted $K_d(490)$ with 21.65% MRE, which was 3.92% and 12.29% lower than the MREs of the IOPK and NOKM models, respectively. The superiority of the updated-NFKM model was very pronounced at high $K_d(490)$. For example, when we applied updated-NFKM to $K_d(490) > 1.0 \text{ m}^{-1}$, most of the points of the field-measured vs. model-derived $K_d(490)$ scatterplot were around the 'one-to-one' line. The slope of the linear relationship between field-measured and model-predicted $K_d(490)$ was 1.01, and the corresponding R^2 was 0.93, meaning that the updated-NFKM model accounted for 93% of the variation of $K_d(490)$, which was 12% and 38% higher than the IOPK and NOKM models' R^2 , respectively. These findings imply that, although the IOPK and updated-NFKM models can predict $K_d(490)$ for global oceanic and coastal waters, the updated-NFKM model's estimates would be more accurate than the IOPK model's estimates.

It is noteworthy that the updated-NFKM model could not produce highly accurate results ($MRE = 42.71\%$, $n = 33$) for measured $K_d(490) < 0.021 \text{ m}^{-1}$, even though the model is much more accurate than the NOKM and IOPK models. As a matter of fact, for extremely clear water, the strong absorption by the water and weak backscattering by the optically active constituents greatly reduce the magnitude of the recorded signal at visible

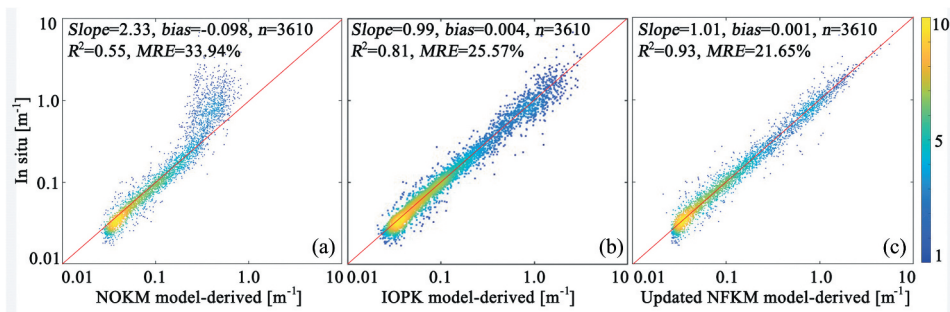


Figure 3. Scatterplots comparing $K_d(490)$: (a) NOKM model, (b) IOPK model, and (c) updated-NFKM model whose architecture had two hidden layers that had 10×12 neurons.

wavelengths thereby reducing the signal-to-noise ratio and enhancing the effect of the inherent noise in the record (Chen et al. 2014), all of which can impact the model's outputs. Consequently, it is at least equally likely that the poor predictions of the updated-NFKM and IOPK models for low $K_d(490)$ results from extremely large amounts of noise in $K_d(490)$ and the remote sensing reflectance derived from radiometric measurements near the sea surface for extremely clear water.

3.2. Evaluating the MODISA and SeaWiFS -derived $K_d(490)$ products

For ocean colour remote sensing, the atmosphere makes up $\sim 90\%$ of the received signal and must be accurately modelled and removed (He et al. 2018). In this study, we used the NASA official atmospheric correction method (Gordon 2019) to minimize atmospheric effects on the water-leaving signals. We used Bailey and Werdell's procedure (2006) to generate synchronous pairs of two different satellite-derived remote sensing reflectance signals used to predict $K_d(490)$. Due to the superiority of the updated-NFKM model over the NOKM and IOPK models in deriving $K_d(490)$ (Chen et al. 2015), we only discuss the updated-NFKM model-based satellite $K_d(490)$ products. We fed the synchronized satellite-observed $R_{rs}(\lambda)$ and $K_d(490)$ data collected from SeaBASS and the eastern China coastal zones into the updated-NFKM model to generate the $K_d(490)$ products, and we evaluated the accuracy of the satellite-derived $K_d(490)$ by comparing the field-observed $K_d(490)$ with the satellite-retrieved $K_d(490)$.

Figure 4 shows how well the updated-NFKM model derived $K_d(490)$ from the MODISA and SeaWiFS satellite-observed remote sensing reflectance after atmospheric correction (Gordon 2019; Gordon and Voss 1999), and we deemed that the updated-NFKM model was acceptably accurate in deriving $K_d(490)$ from the global oceanic and coastal waters. The slopes of the linear relationships between the field-measured and satellite-predicted $K_d(490)$ were 1.03 to 1.19, while the corresponding R^2 s were > 0.84 so that using updated-NFKM model, the SeaWiFS and/or MODISA satellite-detected signals accounted for $> 84\%$ of the variation of $K_d(490)$. Furthermore, the SeaWiFS satellite-predicted $K_d(490)$ was more accurate than the $K_d(490)$ retrieved from the MODISA satellite data. Using SeaWiFS satellite data decreased the MRE by 5.35% over the MODISA satellite data. These results could be because the SeaWiFS sensor was a well-calibrated and stable sensor, and the MODISA data were of lower quality due to several artefacts reported in the sensor's design (Zhang et al. 2006).

3.3. Global view of the uncertainty of the updated-NFKM-derived $K_d(490)$

We present the characteristics of the spatial distribution of the $K_d(490)$ retrieval uncertainty to demonstrate how well the updated-NFKM model quantifies $K_d(490)$, which was calculated by comparing the satellite-derived $K_d(490)$ values with field-measured $K_d(490)$ values. Finally, we used spline interpolation to map the global spatial distribution of the uncertainty using the discrete points of our nine independent datasets. Figure 5 shows the RE of the derived $K_d(490)$ using the updated-NFKM model. The updated-NFKM model overestimated $K_d(490)$ for the open oceans, and the model underestimated, the $K_d(490)$ around the continental shelves. By comparison, the updated-NFKM model did well in deriving the $K_d(490)$ from the Western Pacific, Arctic Ocean, and the North Atlantic to the East Pacific, Southern Ocean, and South Atlantic. Compared to Chen et al. (2015), we found that large RE usually occurred around the regions with low $K_d(490)$. Actually, the

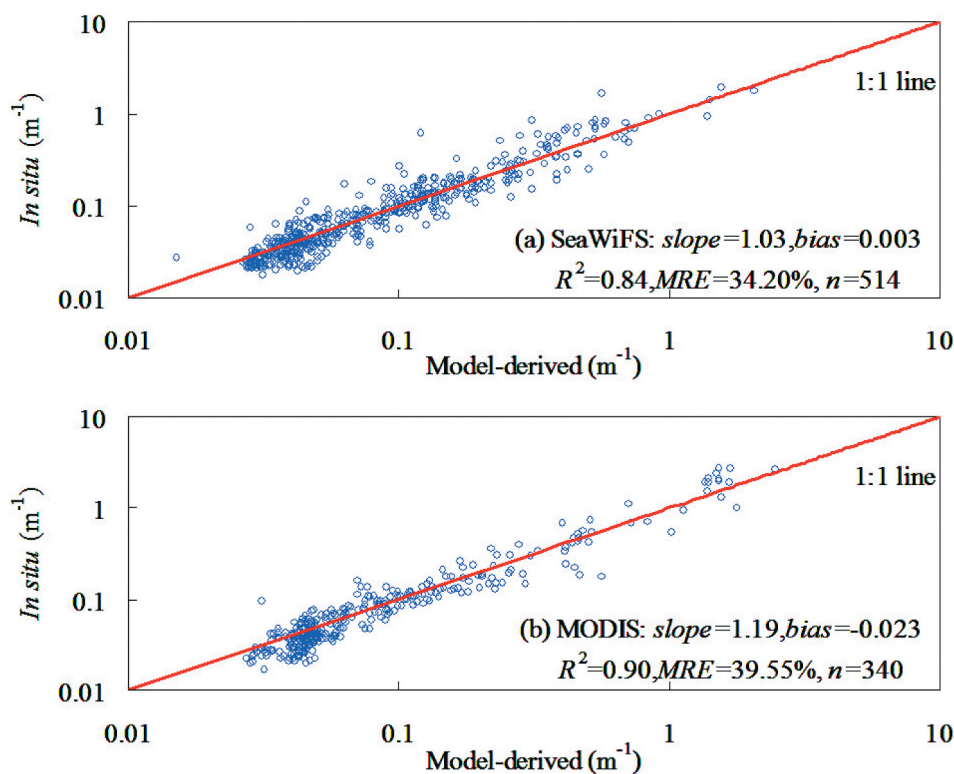


Figure 4. Scatterplots of the $K_d(490)$ estimates using the updated-NFKM model from (a) SeaWiFS and (b) MODIS data versus the synchronized field-measured $K_d(490)$.

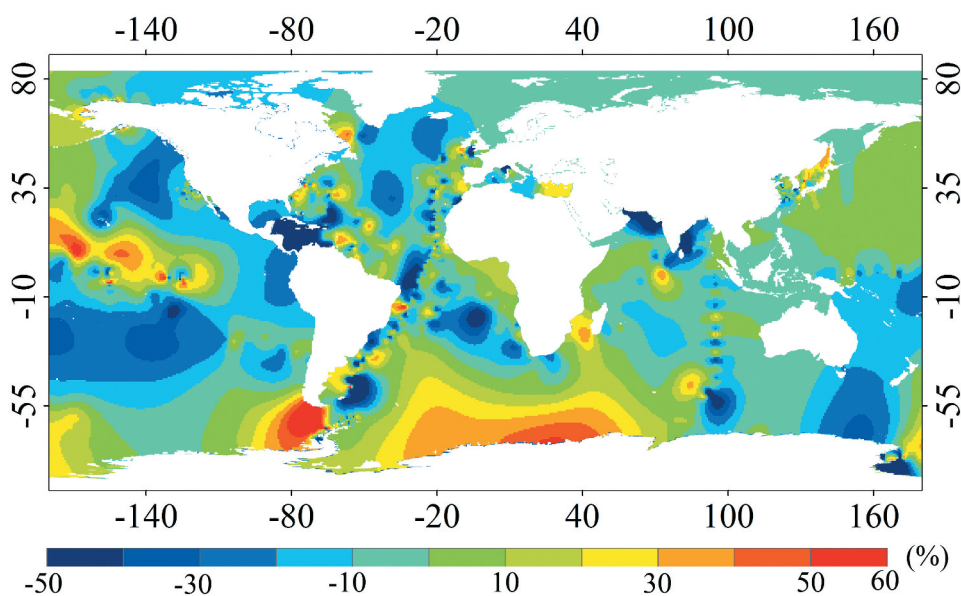


Figure 5. The RE of the updated-NFKM model when deriving $K_d(490)$.

water masses in the open oceans are usually much clearer than those around the coastal zones. The lower magnitudes of the remote sensing reflectance also means that the model is more susceptible to the effects of inherent noises.

Figure 5 also indicates that more than 40% of the global ocean had an absolute relative $K_d(490)$ error well under 10%, and more than 80% of the global ocean had an absolute RE value lower than 30%. These results imply that the updated-NFKM model can accurately derive $K_d(490)$ from satellite-observed or field-measured remote sensing reflectance. Although the geographic coverage of our dataset was quite wide, it might still not have been enough to cover the entire global ocean. For example, there were few available field measurements for some South Hemisphere oceans. Therefore, it would not be logically robust to discuss the uncertainty of the updated-NFKM model regarding global ranges. However, in our present circumstances, there were no available publicly shared datasets more perfect than our datasets for determining the spatial distribution characteristics of the updated-NFKM model's retrieval uncertainty. Therefore, even though we were limited by the spatial coverage of our datasets, these datasets were still beneficial for improving our understanding about how well the updated-NFKM model derives $K_d(490)$ from global oceanic and coastal waters.

3.4. Cross-calibration between MODISA and SeaWiFS data

3.4.1. Daily $K_d(490)$ cross-calibration model

The MODISA and SeaWiFS sensors differed in the way they sampled pixels along- and cross-track. A feature simultaneously observed by these sensors is represented by a slightly different number of image pixels due to the differences in viewing geometry and sensor scanning times. This makes it very difficult to establish sufficient geometric control to compare products on a point-by-point basis. To overcome this difficulty, we used the approach proposed by Bailey and Werdell (2006) to generate synchronized pairs for match-up analysis. We fed 695 pairs consisting of synchronized SeaWiFS- and MODISA- observed remote sensing reflectance collected from SeaBASS into the updated-NFKM model to generate the $K_d(490)$ products required for our cross-calibration for which we established an empirical cross-calibration model.

Figure 6 compares the daily MODISA-predicted with the SeaWiFS-predicted $K_d(490)$. There are differences in the $K_d(490)$ predictions between the two different

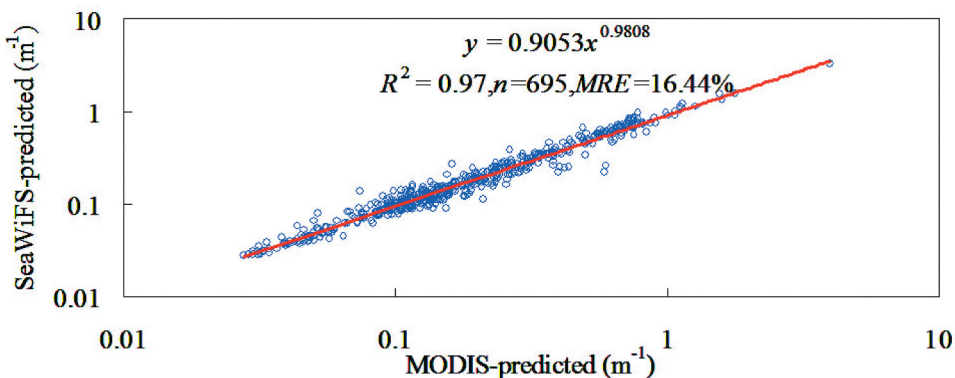


Figure 6. Comparison between the synchronized daily MODISA- and SeaWiFS- predicted $K_d(490)$ for the global oceanic and coastal waters.

satellites. For example, the daily MODISA $K_d(490)$ are slightly larger than the SeaWiFS $K_d(490)$ for $K_d(490) > 0.79 \text{ m}^{-1}$. Because the daily SeaWiFS $K_d(490)$ were more accurate than the MODISA-predicted daily products, we used the SeaWiFS product as the reference sensor, and then we calibrated the daily MODISA-predicted $K_d(490)$ with respect to the SeaWiFS-predicted $K_d(490)$. Finally, we used a power function to simulate the relationship between the daily MODISA- and SeaWiFS- predicted $K_d(490)$. In Figure 6, we see that the relationship between the daily $K_d(490)$ products predicted by the two different sensors could be linked by a power function, whose R^2 was 0.97, which means that using the daily MODISA-predicted $K_d(490)$ accounted for 97% variations of the daily SeaWiFS-predicted $K_d(490)$.

3.4.2. The monthly cross-calibration model

After cross-calibrating the products using our daily cross-calibration model, the SeaWiFS-predicted monthly mean $K_d(490)$ values were still systematically lower than the MODISA values. To enable a naturally smooth transition from SeaWiFS-observed monthly mean $K_d(490)$ products to MODISA monthly products, we still needed a monthly cross-calibration model. We collected the monthly mean $K_d(490)$ predicted from monthly mean remote sensing reflectance from the MODISA and SeaWiFS satellites to establish a monthly cross-calibration model. As we noted previously, because of the differences in the viewing geometry and sensor scanning times, it was difficult to establish sufficient geometric control to facilitate product comparisons on a point-by-point basis. Moreover, the differences in the scanning times means that there might have been different weather conditions such as cloud cover. However, the effects of differing weather conditions could be considered random accidents with equal probability of occurring as the MODISA or SeaWiFS sensor passed as long as there were enough observations. If one accepted this assumption, the global mean $K_d(490)$ along the same latitude from monthly products (latitude-averaged $K_d(490)$) observed by SeaWiFS might be like the MODISA monthly means. As a result, we used the MODISA- and SeaWiFS- predicted latitude-averaged $K_d(490)$ pairs to establish our monthly cross-calibration model.

Figure 7 compares the MODISA-predicted with the SeaWiFS-predicted latitude-averaged $K_d(490)$ for global oceanic and coastal waters. We found that there were biases between the MODISA- and SeaWiFS- predicted latitude-averaged $K_d(490)$ due to the differences in the along- and cross- track pixel sampling. Fortunately, the relationship between the MODISA- and SeaWiFS- predicted latitude-averaged $K_d(490)$ could be described well using an empirical power function, whose R^2 was 0.86. That is, the MODISA-predicted latitude-averaged $K_d(490)$ accounted for 86% of the variations of the SeaWiFS values. However, there were some points far from the curve of the power function in Figure 7. These unexpected scatterplot points could have been caused by the different weather conditions during different satellite transit times (Bailey and Werdell 2006). However, viewed at global scales, the differences between the MODISA- and SeaWiFS- predicted latitude-averaged $K_d(490)$ were very stable and could be systematically corrected using the empirical power function as shown in Figure 7.

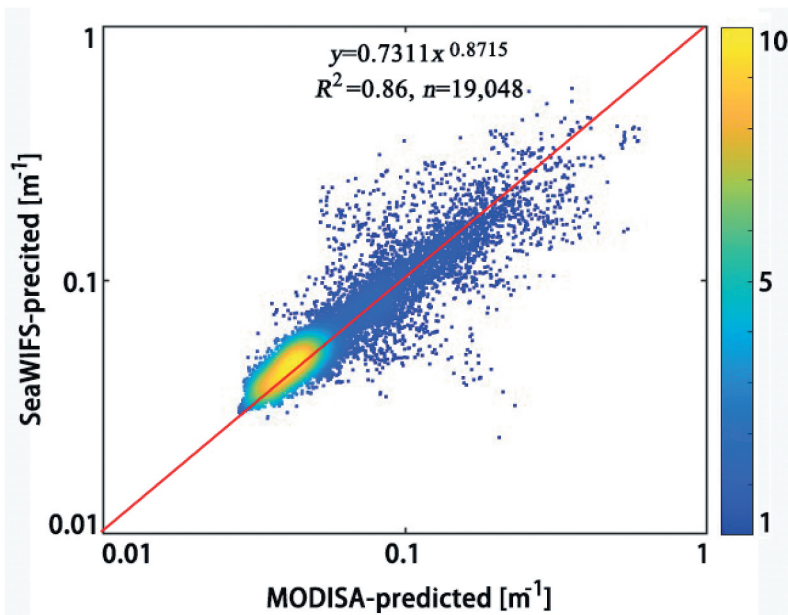


Figure 7. Comparison between the MODISA- and SeaWiFS- predicted latitude-averaged $K_d(490)$ for the global oceanic and coastal waters.

3.5. Global views of the spatial and temporal variations of $K_d(490)$

We used the updated-NFKM model to derive the climatological monthly mean $K_d(490)$ from the monthly mean SeaWiFS- (September 1997 to June 2002) and MODISA- observed (July 2002 to July 2014) remote sensing reflectance from September 1997 to July 2014 for global oceanic and coastal waters. Then, we calculated the latitude-averaged $K_d(490)$ from the MODISA- and SeaWiFS- predicted $K_d(490)$ at global scales. Finally, we used the monthly cross-calibration model to smooth the transition from the MODISA- to SeaWiFS- predicted latitude-averaged $K_d(490)$. Figure 8 shows the monthly variations of $K_d(490)$ along different latitudes from September 1997 to July 2014.

As expected, several features could be found in the map. $K_d(490)$ had strong inter-annual and seasonal variations. This feature is clear in the North and South Hemispheres, especially in the higher latitudes of the North Hemisphere (72°N to 75°N). For example, $K_d(490)$ reached 1.0 m^{-1} from 1998 to 2001 and then decreased to 0.2 m^{-1} from 2004 to 2008. One interesting point was that the annual variation in the northern hemisphere seemed in phase with the annual variation in the southern hemisphere. For example, high $K_d(490)$ from 1998 to 2002 could also be found in the southern hemisphere. The mechanisms causing this in-phase change is interesting, but it is beyond the scope of this paper to discuss the mechanisms. Furthermore, we see that there were seasonal variations. In low latitude oceans (20°N to 40°N) and in the northern hemisphere, $K_d(490)$ in summer (July to September) were lower than for other seasons (Winter: January to March; Spring: April to June; Fall: October to December). As the latitude increased (40°N to 75°N), $K_d(490)$ was low in winter, and the annual peak of $K_d(490)$ moved from spring to fall. Overall, the spatial variation of $K_d(490)$ increased from low latitudes to the high latitudes. This spatial

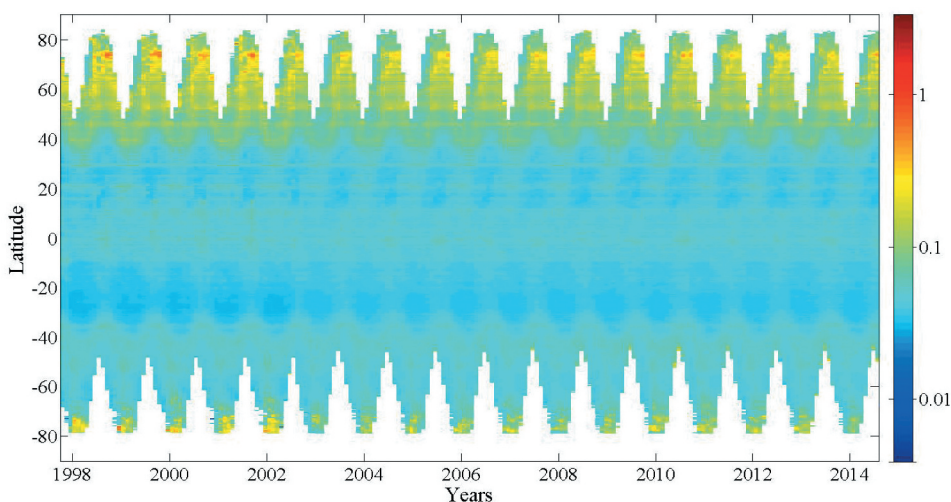


Figure 8. Along-latitude monthly variations of $K_d(490)$ from September 1997 to July 2014.

variation was opposite to the solar radiation trend, which, in general, decreased from the Equator to the poles. As we know, higher $K_d(490)$ traps more solar radiation in the upper oceanic layer for the same magnitude radiation intensity (Wu et al. 2007). This fact implies that oceans at high latitudes could possess equivalent energy in the surface layer for photosynthesis even when the solar intensity is low.

4. Discussion

We demonstrated that the diffuse attenuation coefficient depends on inherent optical properties (Aas 1987; Mobley 1994) and on the variations of solar zenith angle (Austin and Petzold 1981; Z. P. Lee, Du, and Arnone 2005). As a result, viewing a similar water mass at different local times, the model-retrieved $K_d(490)$ values would be different, due to the fact that the solar zenith angle varied with the local time. As we known, the designed satellite transit local time was 12:20 PM for SeaWiFS but 13:20 PM for MODISA. The differences in the satellite transit local times made the solar zenith angles of SeaWiFS smaller than MODISA angles, which in turn lead to the MODISA-predicted daily $K_d(490)$ being slightly higher than those of SeaWiFS (Z. P. Lee, Du, and Arnone 2005). Fortunately, the differences between the MODISA- and SeaWiFS- predicted daily $K_d(490)$ could be deemed to be systematic biases, and could be minimized using the daily cross-calibration model proposed in this study. Our study indicates that using a daily calibration model combined with daily MODISA-predicted $K_d(490)$ could account for 97% variations of the daily SeaWiFS-predicted $K_d(490)$ for the global oceanic and coastal waters.

Scale transformation of remote sensing information is not only a difficult point, but also a hot topic in studies of remote sensing scale. During both analysis and application of remote sensing information, remote sensing information often needs to be transformed among different time scales to achieve integration of multi-temporal remote sensing information and practical application. Due to the nonlinear properties of the updated-NFKM model, the monthly mean $K_d(490)$ was not equal to the results of the updated-

NFKM model derived from the monthly mean remote sensing reflectance. As a result, the daily cross-calibration model would be violated in smoothing the transition from the MODISA-predicted to the SeaWiFS-predicted monthly mean $K_d(490)$. These findings imply that the empirical coefficients of cross-calibration models should be adjusted according to the time and spatial scale characteristics of the $K_d(490)$ products. Judging the data quality by their spatial continuity and image smoothness as shown in [Figure 8](#), our monthly cross-calibration model performed well at changing the MODISA-predicted to the SeaWiFS-predicted latitude-averaged $K_d(490)$.

In [Figure 8](#), we see that the highest annual latitude-averaged $K_d(490)$ were around 75°N in August. At this time, the Arctic Ocean's sea ice cover was disproportionately important to the annual variations of $K_d(490)$ in the high-latitude regions because the sea ice provided a physical boundary with gas exchange between the atmosphere and ocean and was an ecologically important habitat for the algal community (Yamamoto et al. 2014). In general, during spring, most of the Arctic Ocean is covered by sea ice, which makes it difficult for the solar irradiance to penetrate into the ocean, and the phytoplankton growth becomes light-limited (Hill and Zimmerman 2010). As the ocean surface temperature rises during the summer and autumn, the sea ice begins to melt and release nutrients required for phytoplankton growth (Pirtle-Levy et al. 2009), which results in algal blooms in the late summer and early autumn (Serreze, Holland, and Stroeve 2007). In the winter, the ice-free ocean shrinks due to the decreasing ocean temperature (Huck et al. 2007), even though the nutrient levels are still very high after the autumn algal bloom (Hill and Zimmerman 2010). However, due to light limitation in autumn, phytoplankton concentrations are still extremely low. As we know, $K_d(490)$ is constrained by the concentrations of phytoplankton, dissolved yellow substances, and suspended particulate matter. Therefore, the spatial and temporal changes of $K_d(490)$ in the Arctic Ocean would have been constrained by the changes in the sea ice cover.

Over the past several decades, many reports attributed the intermission difference in ocean colour products to satellite measurement uncertainty caused by internal factors of sensor performance and data processing procedures (Chen et al. 2020; Pahlevan, Sarkar, and Franz 2016; Savtchenko et al. 2004; Zibordi, Mélin, and Berthon 2012). In general, accepted theory assumed that observed bio-optical properties remained unchanged within several hours of observation (Bailey and Werdell 2006), so the intermission difference associated with the data processing procedures could be removed. However, the optically activity components such as phytoplankton have the significant diurnal cycle pattern correlated with the day-night cycle in light and nutrients (Suzuki and Johnson 2010), which has been confirmed for several oceanic regions such as the western equatorial Pacific (Arata et al. 1996), the equatorial Pacific (Neveux et al. 2003), the Bay of Bengal (Prasanth, Vijith, and Vinayachandran 2023), and the Gulf of Mexico (Arnone et al. 2017). Thus, it is not easy to combine the morning and afternoon satellite for long-term application unless we could remove the diurnal variation.

Importantly, the Raman factor was mainly developed for removing the Raman-scattering contributions in the open oceans (Z. Lee et al. 2013), which might be violated in the turbid coastal waters. Chen et al. (2016) suggested that when the neural network models were trained using data including residual errors, it can absorb some impacts of the

residual errors for ocean colour estimations. This was to say, the Raman factor might be unable to accurately remove Raman-scattering effect in the turbid waters, but it would not lead to poor result that the updated-NFKM model was not effective in $K_d(490)$ estimation in these waters.

5. Summary

In our study, we discussed the accuracy and consistency of MODISA and SeaWiFS $K_d(490)$ estimates, which have been reported very little in the literature. We evaluated the accuracies of three existing $K_d(490)$ models run with MODISA and SeaWiFS data using field measurements taken from nine different datasets. By comparing our results with in situ measurements, using the NOKM model, we found that $K_d(490)$ was slightly over-estimated at exceptionally low values, and were significantly underestimated at high values. By comparison, the IOPK and updated-NFKM models were better able to retrieve $K_d(490)$ for global oceanic and coastal waters, but the updated-NFKM model was slightly more accurate than the NOKM and IOPK models. Using the updated-NFKM model decreased the MRE by $> 4\%$ compared to the NOKM and IOPK models. We also presented a global view of the uncertainty of the updated-NFKM model for estimating $K_d(490)$. The results showed that the updated-NFKM model performed better for the Western Pacific, Arctic Ocean, and Northern Atlantic compared to the Eastern Pacific, Southern Ocean, and South Atlantic.

We quantified $K_d(490)$ from MODISA and SeaWiFS images after performing an atmospheric correction using the NASA official standard atmospheric correction. After comparing the satellite-predicted to the field-measured $K_d(490)$, we found that the updated-NFKM model produced $\text{MRE} < 40\%$ in deriving $K_d(490)$ from the MODISA and SeaWiFS. By comparison, the SeaWiFS satellite-predicted $K_d(490)$ had 5.35% MRE more accurate than the MODISA satellite-predicted $K_d(490)$. Moreover, we found that there were some differences between the SeaWiFS- and MODISA- predicted $K_d(490)$. For example, the $K_d(490)$ values retrieved from the MODISA data were slightly higher than those retrieved from the SeaWiFS data. Using the SeaWiFS sensor as the reference sensor, we minimized the biases between the MODISA- and SeaWiFS- predicted $K_d(490)$ using our cross-calibration model. However, due to scaling effects of the $K_d(490)$ retrieval model, the empirical coefficients of the cross-calibration model changed with time scales of the composite remote sensing reflectance. Finally, we applied the updated-NFKM model and cross-calibration model to briefly illuminate the monthly variations of $K_d(490)$ from 1997 to 2014 for global oceans. The results indicate that the maximum latitude-averaged $K_d(490)$ was at high latitudes during August, and the minima were around mid-latitudes during March.

Disclosure statement

No potential conflict of interest was reported by the author(s).

Funding

The National Natural Science Foundation of China [42022045, Chen], and Shan'xi Key Research and Development Program [2022ZDLSF06-09, Chen] provided financial support for this study.

References

- Aas, E. 1987. "Two-stream irradiance model for deep waters." *Applied Optics* 11 (11): 2095–2101. <https://doi.org/10.1364/AO.26.002095>.
- Aiken, J., G. F. Moore, C. C. Trees, S. B. Hook, and D. K. Clark. 1995. "The SeaWiFS CZCS-Type Pigment Algorithm." *SeaWiFS Technical Report Series*. 29. Greenbelt, MD: Goddard Space Flight Center.
- Arata, K., Z.-H. Xiao-Hua, and M.-H. Radenac. 1996. "Diurnal Variability and Its Quantification of Subsurface Sound Scatterers in the Western Equatorial Pacific." *Journal of Oceanography* 52 (5): 655–674. <https://doi.org/10.1007/BF02238326>.
- Arnone, R., R. Vandermuelen, I. Soto, S. Ladner, M. Ondrusek, and H. Yang. 2017. "Diurnal Changes in Ocean Color Sensed in Satellite Imagery." *Journal of Applied Remote Sensing* 11 (3): 032406. <https://doi.org/10.1117/1.JRS.11.032406>.
- Austin, R. W., and T. Petzold. 1981. *The Determination of the Diffuse Attenuation Coefficient of Sea Water Using the Coastal Zone Colour Scanner*. 239–256. New York: Springer.
- Bailey, S. W., and P. J. Werdell. 2006. "A Multi-Sensor Approach for the On-Orbit Validation of Ocean Color Satellite Data Products." *Remote Sensing of Environment* 102 (1–2): 12–23. <https://doi.org/10.1016/j.rse.2006.01.015>.
- Barale, V. 1987. "Remote Observations of the Marine Environment: Spatial Heterogeneity of the Mesoscale Ocean Color Field in CZCS Imagery of California Near-Coastal Waters." *Remote Sensing of Environment* 22 (2): 173–186. [https://doi.org/10.1016/0034-4257\(87\)90057-5](https://doi.org/10.1016/0034-4257(87)90057-5).
- Chen, J., T. W. Cui, J. Ishizaka, and C. S. Lin. 2014. "A Neural Network Model for Remote Sensing of Diffuse Attenuation Coefficient in Global Oceanic and Coastal Waters: Exemplifying the Applicability of the Model to the Coastal Regions in Eastern China Seas." *Remote Sensing of Environment* 148:168–177. <https://doi.org/10.1016/j.rse.2014.02.019>.
- Chen, J., X. He, X. Xing, Q. Xing, Z. Liu, and D. Pan. 2020. "An Inherent Optical Properties Data Processing System for Achieving Consistent Ocean Color Products from Different Ocean Color Satellites." *Journal of Geophysical Research Oceans* 125 (1): e2019JC015811. <https://doi.org/10.1029/2019JC015811>.
- Chen, J., J. Ishizaka, L. Y. Zhu, T. W. Cui, J. Ishizaka, and Y. Ju. 2015. "A Neural Network Model for $K(\lambda)$ Retrieval and Application to Global Kpar Monitoring." *PLoS One* 10 (6): 0127511–0127526. <https://doi.org/10.1371/journal.pone.0127514>.
- Chen, J., Z. P. Lee, C. M. Hu, and J. W. Wei. 2016. "Improving Satellite Data Products for Open Oceans with a Scheme to Correct the Residual Errors in Remote Sensing Reflectance." *Journal of Geophysical Research: Ocean* 121 (6): 3866–3886. <https://doi.org/10.1002/2016JC011673>.
- Clavano, W. R., E. Boss, and K. B. Lee. 2007. "Inherent Optical Properties of Non-Spherical Marine-Like Particles—From Theory to Observation." *Oceanography and Marine Biology* 45:1–38.
- Dall'olmo, G., A. A. Gitelson, D. C. Rundquist, B. Leavitt, T. Barrow, and J. C. Holz. 2005. "Assessing the Potential of SeaWiFS and MODIS for Estimating Chlorophyll Concentration in Turbid Productive Waters Using Red and Near-Infrared Bands." *Remote Sensing of Environment* 96 (2): 176–187. <https://doi.org/10.1016/j.rse.2005.02.007>.
- Gordon, H. R. 2019. *Physical Principles of Ocean Color Remote Sensing*. Coral Gables, FL, USA: University of Miami. <https://doi.org/10.33596/ppocrs-19>.
- Gordon, H. R., and K. J. Voss. 1999. "Normalized Water-Leaving Radiance." In *MODIS Algorithm Theoretical Basis Document (ATBD-17)*. 1–2. NASA.
- He, X., K. Stamnes, Y. Bai, W. Li, and D. Wang. 2018. "Effects of Earth Curvature on Atmospheric Correction for Ocean Color Remote Sensing." *Remote Sensing of Environment* 209:118–133. <https://doi.org/10.1016/j.rse.2018.02.042>.
- Hill, V. J., and R. C. Zimmerman. 2010. "Estimates of Primary Production by Remote Sensing in the Arctic Ocean: Assessment of Accuracy with Passive and Active Sensors." *Deep Sea Research Part I* 57 (10): 1243–1254. <https://doi.org/10.1016/j.dsr.2010.06.011>.
- Huang, C., and L. Yao. 2017. "Semi-Analytical Retrieval of the Diffuse Attenuation Coefficient in Large and Shallow Lakes from GOCI, a High Temporal-Resolution Satellite." *Remote Sensing* 9 (8): 825. <https://doi.org/10.3390/rs9080825>.

- Huck, P., B. Light, H. Eicken, and M. Haller. 2007. "Mapping Sediment-Laden Sea Ice in the Arctic Using AVHRR Remote Sensing Data: Atmospheric Correction and Determination of Reflectances as a Function of Ice Type and Sediment Load." *Remote Sensing of Environment* 107 (3): 484–495. <https://doi.org/10.1016/j.rse.2006.10.002>.
- IOCCG. 2006. "Remote Sensing of Inherent Optical Properties: Fundamentals, Tests of Algorithms, and Applications." *Reports of the International Ocean Colour Coordinating Group No.5, Dartmouth, Canada: IOCCG*.
- Lee, Z. P., K. L. Carder, and R. A. Arnone. 2002. "Deriving Inherent Optical Properties from Water Color: A Multi-Band Quasi-Analytical Algorithm for Optically Deep Waters." *Applied Optics* 41 (27): 5755–5772. <https://doi.org/10.1364/AO.41.005755>.
- Lee, Z. P., K. P. Du, and R. A. Arnone. 2005. "A Model for the Diffuse Attenuation Coefficient of Downwelling Irradiance." *Journal of Geophysical Research* 110 (C2): C02017. <https://doi.org/10.1029/2004JC002275>.
- Lee, Z., C. Hu, S. Shang, K. Du, M. Lewis, R. Arnone, and R. Brewin. 2013. "Penetration of UV-Visible Solar Radiation in the Global Oceans: Insights from Ocean Color Remote Sensing." *Journal of Geophysical Research Oceans* 118 (9): 4241–4255. <https://doi.org/10.1002/jgrc.20308>.
- Masini, R. J., J. L. Cary, C. J. Simpson, and A. J. McComb. 1995. "Effects of Light and Temperature on the Photosynthesis of Temperate Meadow-Forming Seagrasses in Western Australia." *Aquatic Botany* 49 (4): 239–254. [https://doi.org/10.1016/0304-3770\(94\)00432-L](https://doi.org/10.1016/0304-3770(94)00432-L).
- Meister, G., B. A. Franz, E. J. Kwiatkowska, and C. McClain. 2012. "Correction to the Calibration of MODIS Aqua Ocean Color Bands Derived from SeaWiFS Data." *IEEE Transaction on Geoscience and Remote Sensing* 50 (1): 310–319. <https://doi.org/10.1109/TGRS.2011.2160552>.
- Mélin, F. 2016. "Impact of Inter-Mission Differences and Drifts on Chlorophyll-A Trend Estimates." *International Journal of Remote Sensing* 37 (10): 2061–2079. <https://doi.org/10.1080/01431161.2016.1168949>.
- Mélin, F., G. Sclep, T. Jackson, and S. Sathyendranath. 2016. "Uncertainty Estimates of Remote Sensing Reflectance Derived from Comparison of Ocean Color Satellite Data Sets." *Remote Sensing of Environment* 177:107–124. <https://doi.org/10.1016/j.rse.2016.02.014>.
- Mobley, C. D. 1994. *Light and Water: Radiative Transfer in Natural Waters*. New York: Academic Press.
- Mueller, J. L. 2000. "SeaWiFS Algorithm for the Diffuse Attenuation Coefficient, Kd(490), Using Water-Leaving Radiance at 490 and 555 Nm." *SeaWiFS Postlaunch Calibration and Validation Analysis: Part II 3* (11): 24–27.
- Mueller, J. L., C. O. Davis, R. A. Arnone, R. Frouin, K. L. Carder, Z. P. Lee, R. G. Steward, S. Hooker, C. D. Mobley, and C. R. McClain. 2003. "Above-water radiance and remote sensing measurement and analysis protocols." *Ocean Optics Protocols for Satellite Ocean-Color Sensor Validation, Revision 4, Vol. III: Radiometric Measurements and Data Analysis Protocols*. 21162. NASA Tech Memo.
- Mueller, J. L., and G. S. Fargion. 2002. "Ocean optics protocols for satellite ocean color sensor validation." *SeaWiFS Technical Report Series, Revision 3 Part II*. 171–179.
- Mueller, J. L., and C. C. Trees. 1997. "Revised SeaWiFS Prelaunch Algorithm for Diffuse Attenuation Coefficient K(490)." *NASA SeaWiFS Technical Report Series, TM-104566*, 41, 18–21.
- Neveux, J., C. Dupouy, J. Blanchot, A. Le Bouteiller, M. R. Landry, and S. L. Brown. 2003. "Diel Dynamics of Chlorophylls in High-Nutrient, Low-Chlorophyll Waters of the Equatorial Pacific (180°): Interactions of Growth, Grazing, Physiological Responses, and Mixing." *Journal of Geophysical Research Oceans* 108 (C12). <https://doi.org/10.1029/2000JC000747>.
- Pahlevan, N., S. Sarkar, and B. A. Franz. 2016. "Uncertainties in Coastal Ocean Color Products: Impacts of Spatial Sampling." *Remote Sensing of Environment* 181:14–26. <https://doi.org/10.1016/j.rse.2016.03.022>.
- Pedersen, T. M., C. L. Gallegos, and S. L. Nielsen. 2012. "Influence of Near-Bottom Re-Suspended Sediment on Benthic Light Availability." *Estuarine, Coastal and Shelf Science* 106:93–101. <https://doi.org/10.1016/j.ecss.2012.04.027>.
- Pirtle-Levy, R., J. M. Grebmeier, L. W. Cooper, and L. Larsen. 2009. "Chlorophyll a in Arctic Sediments Implies Long Persistence of Algal Pigments." *Deep-Sea Research* 56 (17): 1326–1338. <https://doi.org/10.1016/j.dsr2.2008.10.022>.

- Prasanth, R., V. Vijith, and P. N. Vinayachandran. 2023. "Formation, Maintenance and Diurnal Variability of Subsurface Chlorophyll Maximum During the Summer Monsoon in the Southern Bay of Bengal." *Progress in Oceanography* 212:102974. <https://doi.org/10.1016/j.pocean.2023.102974>.
- Sathyendranath, S., R. J. W. Brewin, C. Brockmann, V. Brotas, B. Calton, A. Chuprin, P. Cipollini, et al. 2019. *An Ocean-Colour Time Series for Use in Climate Studies: The Experience of the Ocean-Colour Climate Change Initiative (OC-CCI)*. Basel, Switzerland: Sensors.
- Saulquin, B., A. Hamdi, F. Gohin, J. Populus, A. Mangin, and O. F. d'Andon. 2013. "Estimation of the Diffuse Attenuation Coefficient KdPar Using MERIS and Application to Seabed Habitat Mapping." *Remote Sensing of Environment* 128:224–233. <https://doi.org/10.1016/j.rse.2012.10.002>.
- Savtchenko, A., D. Ouzounov, S. Ahmad, J. Acker, G. Leptoukh, J. Koziana, and D. Nickless. 2004. "Terra and Aqua MODIS Products Available from NASA GES DAAC." *Advances in Space Research* 34 (4): 710–714. <https://doi.org/10.1016/j.asr.2004.03.012>.
- Serreze, M. C., M. M. Holland, and J. Stroeve. 2007. "Perspectives on the Arctic's Shrinking Sea-Ice Cover." *Science* 315:1533–1536. <https://doi.org/10.1126/science.1139426>.
- Suzuki, L., and C. H. Johnson. 2010. "Algae Know the Time of Day: Circadian and Photoperiodic Programs." *Journal of Phycology* 37 (6): 933–942. <https://doi.org/10.1046/j.1529-8817.2001.01094.x>.
- Werdel P. J., and S. W., Bailey. 2005. "An improved bio-optical data set for ocean color algorithm development and satellite data product variation." *Remote Sensing of Environment* 98 (1): 122–140. <https://doi.org/10.1016/j.rse.2005.07.001>.
- Wu, Y. T., S. Platt, T. Sathyendranath, and T. Platt. 2007. "The Impact of Bio-Optical Heating on the Properties of the Upper Ocean: A Sensitivity Study Using a 3-D Circulation Model for the Labrador Sea." *Deep Sea Research Part II* 54 (23–26): 2630–2642. <https://doi.org/10.1016/j.dsr2.2007.08.019>.
- Xing, X., F. Zhang, E. Boss, and J. Chai. 2020. "Evaluation of ocean color remote sensing algorithms for diffuse attenuation coefficients and optical depths with data collected on BGC-Argo floats." *Remote Sensing* 12 (15): 2367. <https://doi.org/10.3390/rs12152367>.
- Yamamoto, S., C. Michel, M. Gosselin, S. Demers, M. Fukuchi, and S. Taguchi. 2014. "Photosynthetic Characteristics of Sinking Microalgae Under the Sea Ice." *Polar Science* 8 (4): 385–396. <https://doi.org/10.1016/j.polar.2014.1007.1007>.
- Zhang, C., C. Hu, S. Shang, F. E. Müller-Karger, Y. Li, M. Dai, and B. Huang. 2006. "Bridging Between SeaWiFS and MODIS for Continuity of Chlorophyll-A Concentration Assessments off Southeastern China." *Remote Sensing of Environment* 102 (3–4): 250–263. <https://doi.org/10.1016/j.rse.2006.02.015>.
- Zhao, J., B. Barnes, N. Melo, D. English, B. Lapointe, F. E. Muller-Karger, B. Schaeffer, and C. M. Hu. 2013. "Assessment of Satellite-Derived Diffuse Attenuation Coefficients and Euphotic Depths in South Florida Coastal Waters." *Remote Sensing of Environment* 131:38–50. <https://doi.org/10.1016/j.rse.2012.12.009>.
- Zibordi, G., F. Mélin, and J.-F. Berthon. 2012. "Intra-Annual Variations of Biases in Remote Sensing Primary Ocean Color Products at a Coastal Site." *Remote Sensing of Environment* 124:627–636. <https://doi.org/10.1016/j.rse.2012.06.016>.